


Valley filtering in black phosphorus nanofilms under a magnetic-electric barrierDewei Chen¹ and Feng Zhai^{1,2,*}¹*Department of Physics, Zhejiang Normal University, Jinhua 321004, China*²*Zhejiang Institute of Photoelectronics, Zhejiang Normal University, Jinhua 321004, China* (Received 12 August 2023; revised 1 December 2023; accepted 4 December 2023; published 18 December 2023)

We investigate valley filtering in black phosphorus (BP) nanofilms modulated by either a pure electric barrier or a magnetic-electric barrier. The considered BP nanofilm has a negative band gap and thus hosts two degenerate Dirac points. We confirm that the system under a pure electric barrier can undergo three distinct valley states as the gate voltage varies. However, the three valley states appear only when the angle β between the transport and the zigzag direction is very close to 0. The absence of intervalley transmission at a finite β disallows pseudospin-selective tunneling, leading to a strictly zero (at $\beta = 90^\circ$) or weak valley polarization. When a magnetic barrier is included, the three valley states under $\beta = 0^\circ$ survive. The magnetic barrier can effectively break the reflection symmetry between the two valleys at β near 90° . Accordingly, one can achieve a remarkable valley polarization with gate-tunable polarity when the transport direction is near the armchair direction. Our findings could be helpful for design valleytronic devices based on two-dimensional systems with merging Dirac cones.

DOI: [10.1103/PhysRevB.108.235425](https://doi.org/10.1103/PhysRevB.108.235425)**I. INTRODUCTION**

The manipulation of valley degrees of freedom in two-dimensional (2D) materials has attracted extensive attention in recent years [1,2]. Valleytronics is expected to offer a routine to the next-generation electronic devices. A key step of valleytronics is to create an uneven population between momentum-distinguishable valleys in the band structure. Valley-polarized current can be generated by breaking the inversion and/or time-reversal symmetry. Thus far, many valley-filtering schemes have been put forward based on 2D materials with honeycomb structures. In monolayered MoS₂ with valley-contrasting Berry curvature, valley polarization was induced experimentally by means of circularly polarized light [3–6]. For graphene placed on a monolayer of hexagonal boron nitride [7], the detected valley Hall currents show a long-range character and transistorlike gate control. In dual-gated bilayer graphene, pure valley current has been generated and detected by nonlocal resistance measurements [8]. Theoretically, valley filtering in a graphene sheet can be achieved by means of strain-induced pseudomagnetic fields [9–12], sublattice-staggered potential [13,14], line defect [15,16], valley-Zeeman effect [17,18], and the application of circularly polarized light [19,20].

Few-layer black phosphorus (BP) has received much attention in recent years due to its stable structure, excellent electrochemical properties [21], electrically tunable band gap [22], and high carrier mobility [23]. In contrast to 2D graphene and MoS₂, BP nanofilms are highly anisotropic, which results in direction-dependent optical and transport properties [24–26]. Recently, it has been found that external perturbations can reduce the band gap of BP nanofilms and

even induce band reversals, where the reversal band gap can reach 0.6 eV [27,28]. When the band gap is reversed, two merging Dirac cones with chiral pseudospins appear [29], which offers a way to valleytronic applications. As demonstrated theoretically in Ref. [30], the transport of one valley can be effectively quenched when its pseudospin direction mismatches that of a gate-controlled scattering region. Such pseudospin-selective quantum tunneling in 2D systems with two degenerate merging Dirac cones can be utilized to design an all-electric-controlled valley filter, valve, and logic gate. Note that the transport direction considered in Ref. [30] is in parallel with the line passing the two Dirac cones (the zigzag direction of BP monolayer). Since the electron energy band of BP nanofilms is highly anisotropic, it is necessary to explore valley-related tunneling features in other transport directions. For junctions made of band-gap-inverted BP, the calculation in Ref. [31] indicates that intervalley tunneling is totally prohibited by momentum conservation in the armchair junction or partially suppressed by pseudospin mismatch in the zigzag junction. However, valley filtering was not concerned in Ref. [31].

In this work we explore the effect of transport direction on the valley filtering in band-gap-inverted BP under the modulation of a pure electric barrier or magnetic-electric barrier. In the considered system the valley index is not conserved and is even ambiguous in some propagating states. There are different ways to define the valley polarization in the presence of intervalley scattering [30,32]. As suggested in Ref. [33], the valley Hall effect in gapped graphene is better described as the orbital Hall effect, where the ambiguous valley index is replaced by the orbital magnetic moment (OMM). Therefore, we adopt the OMM to replace the vague valley index and characterize the valley polarization. We find that the valley polarization under a pure electric barrier decreases rapidly when the transport direction deviates from the zigzag

*fzhai@zjnu.cn

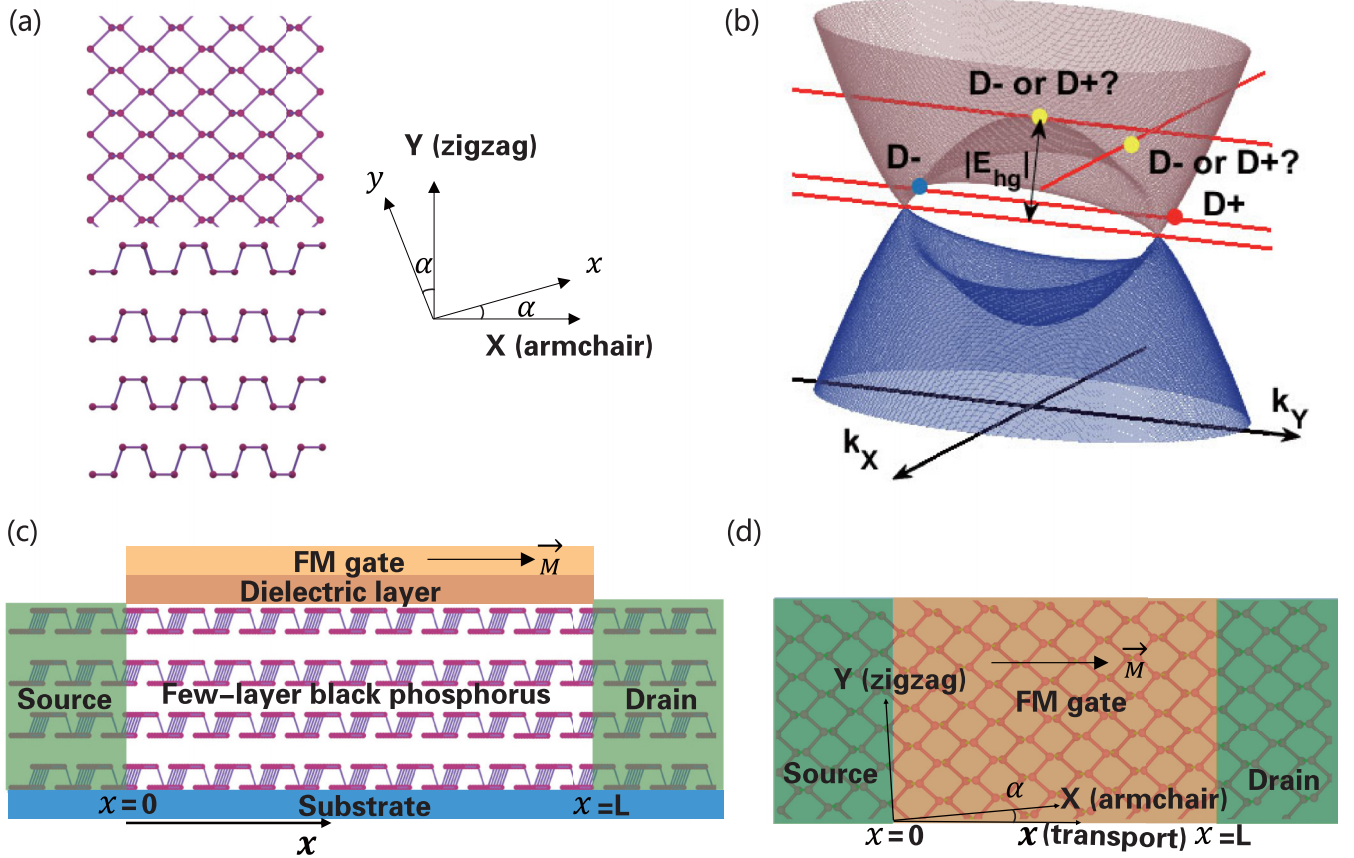


FIG. 1. Energy band structure of a band-inverted BP nanofilm and the considered device. (a) Top and side view of the atomic structure of four-layered BP. The X and Y axis are along an armchair and zigzag direction. (b) Energy band structure of band-inverted BP nanofilm. The solid dots mark the points with a vague valley index. (c) Front view of the considered device: an FM gate with width L is placed on top of a few-layer BP, which generates both a local magnetic field and a gate-tunable electric barrier. The magnetization \vec{M} of the FM gate is along the width direction and has an angle α to the X axis. (d) Top view of the considered device.

direction (by a value 5° or so), which vanishes strictly for the transport along the armchair direction. The strong dependence of valley filtering on the transport direction may limit the valleytronic applications of BP nanofilms with inverted band gap. Fortunately, we find that under a magnetic-electric barrier, remarkable valley polarization can be achieved when the transport direction is near either the zigzag or armchair direction.

II. MODEL AND FORMALISM

For a few-layer BP in the absence of external fields, the electronic structure near the Γ point can be well described by a two-band effective Hamiltonian [27]:

$$\tilde{H}_0(\tilde{k}_X, \tilde{k}_Y) = \hbar v_X \tilde{k}_X \sigma_Y + \left(\frac{\varepsilon_g}{2} + \frac{\gamma \hbar^2 \tilde{k}_X^2}{2m_Y} + \frac{\hbar^2 \tilde{k}_Y^2}{2m_Y} \right) \sigma_Z. \quad (1)$$

Here \tilde{k}_X and \tilde{k}_Y (m_X and m_Y) are the wave vector (effective mass) along the armchair and zigzag directions, respectively [Fig. 1(a)], $\gamma = m_Y/m_X$ is a dimensionless parameter, v_X is the effective velocity along the armchair direction, σ_X , σ_Y , and σ_Z are three Pauli matrices acting on the pseudospin space, and ε_g is the band gap. This $\mathbf{k} \cdot \mathbf{p}$ Hamiltonian without the parabolic term $\hbar^2 \tilde{k}_X^2 / (2m_Y) \sigma_Z$ has been utilized to model

deformed honeycomb lattices with merging Dirac cones [34,35]. For convenience, hereafter we will express all quantities in dimensionless form by means of the energy unit $\varepsilon_0 = 2m_Y v_X^2$ and length unit $l_0 = \hbar / (2m_Y v_X)$. Then Eq. (1) becomes

$$H_0(k_X, k_Y) = k_X \sigma_Y + (E_{hg} + \gamma k_X^2 + k_Y^2) \sigma_Z, \quad (2)$$

where $H_0 = \tilde{H}_0 / \varepsilon_0$, $k_{X,Y} = \tilde{k}_{X,Y} l_0$, and $E_{hg} = \varepsilon_g / (2\varepsilon_0)$.

For an electron with wave vector $\mathbf{k} = k_X \mathbf{e}_X + k_Y \mathbf{e}_Y$ and energy E , one can obtain from Eq. (2) the dispersion relation, eigenstate $u(\mathbf{k}; E)$, and pseudospinor $\mathbf{S}(\mathbf{k}; E)$:

$$E^2 = k_X^2 + Q^2, \quad Q = E_{hg} + \gamma k_X^2 + k_Y^2, \quad (3)$$

$$u(\mathbf{k}; E) = (Q + E, ik_X)^T / \sqrt{2E^2 + 2EQ}, \quad (4)$$

$$\mathbf{S}(\mathbf{k}; E) = u^+(\mathbf{k}; E) \sigma u(\mathbf{k}; E) = \frac{k_X}{E} \mathbf{e}_Y + \frac{Q}{E} \mathbf{e}_Z. \quad (5)$$

The group velocity of this plane-wave state is $\mathbf{v}(\mathbf{k}; E) = \nabla_{\mathbf{k}} E$ and can be expressed as

$$\mathbf{v}(\mathbf{k}; E) = \frac{k_X + 2\gamma Q k_X}{E} \mathbf{e}_X + \frac{2Q k_Y}{E} \mathbf{e}_Y. \quad (6)$$

The band gap ε_g of a BP thin film depends on the number of layers, which ranges from the bulk limit 0.3 eV to the

monolayer limit 1.8 eV [24,36,37]. Note that the band gap ε_g can be inverted by means of pressure [38,39], strain [40], vertical electric field [41–43], and surface doping [28,29,44]. In the case $\varepsilon_g = 2\varepsilon_0 E_{hg} < 0$, one can see from Eq. (3) that the conduction and valence band touch at two points $\mathbf{D}_\pm = (0, \pm k_D)$ with $k_D = \sqrt{-E_{hg}}$.

As seen in Fig. 1(b), two Dirac cones within $|E| < |E_{hg}|$ are formed in the momentum space, which are well separated along the zigzag direction. The two inequivalent Dirac cones provide a twofold valley degeneracy of electrons in few-layer BP, which are denoted as D_+ and D_- valleys in Ref. [30]. Usually the valley index η of a propagating state $u(\mathbf{k}; E)$ is determined by the distance between the wave vector \mathbf{k} and \mathbf{D}_\pm . One assigns $\eta = 1$ (-1) if and only if $|\mathbf{k} - \mathbf{D}_+|$ is smaller (larger) than $|\mathbf{k} - \mathbf{D}_-|$. As shown in Fig. 1(b), this criterion is ambiguous, especially for the points with $k_Y = 0$. The valley polarization of an electric current can be defined from the view of OMM rather than this vague valley indicator [33]. However, the OMM vanishes for the Hamiltonian (2). To circumvent this problem, a gap term $\delta\sigma_X$ is introduced, which represents a negligible gap opening where the constant δ satisfies $0 < \delta \ll 1$. As shown in the Supplemental Material of Ref. [28], the gap term $\delta\sigma_X$ can be introduced by breaking the glide mirror symmetry along the armchair direction of a multilayered phosphorene. Such a gap has indeed been observed in Ref. [45] (see Fig. 4 therein). The band-gap openings at the crossing points in the $\Gamma - X$ and $\Gamma - Y$ crystallographic directions could arise from a random distribution of doped alkali metal atoms, nonzero interlayer interaction, or stacking faults on the BP surface. The OMM $\mathbf{m}(\mathbf{k}, E)$ for the Hamiltonian $H_0 + \delta\sigma_X$ has only one nonzero component $m_z(\mathbf{k}, E)$, which is given by [33,46–48]

$$m_z(\mathbf{k}, E) = -\frac{e}{\hbar} \frac{\delta k_Y \text{sgn}(E)}{\delta^2 + k_X^2 + (E_{hg} + \gamma k_X^2 + k_Y^2)^2}. \quad (7)$$

Here $\text{sgn}(E)$ takes $+1$ (-1) for the conduction (valence) band. The OMM has the largest amplitude at $\mathbf{k} = \mathbf{D}_\pm$ and opposite directions at the two valley points.

For tetralayer BP (TBP) with potential difference between the top and bottom layers, the Hamiltonian parameters are determined in Ref. [27] by a self-consistent Hartree method. In subsequent calculations, we take a set of parameters for TBP given by Ref. [27]: $m_Y = 0.95 m_e$ (m_e is the mass of a free electron in vacuum), $\gamma = 5.2$, $\varepsilon_g = -0.134$ eV, and $v_X = 7.5 \times 10^6$ cm/s. The values of energy and length unit are $\varepsilon_0 \approx 60.76$ meV and $l_0 \approx 0.813$ nm. Accordingly, $E_{hg} = \varepsilon_g/(2\varepsilon_0) = -1.115$.

To generate a valley-polarized current along an arbitrary direction, we consider a device [see Figs. 1(c) and 1(d)] based on TBP with band inversion, where the motion of electrons in the (X, Y) plane is modulated by a magnetic-electric barrier generated by a ferromagnetic gate (FMG) on top. This magnetic barrier has been formed experimentally on traditional two-dimensional electron gas systems [49–52]. The FMG has a rectangular cross section with width L along the x direction. Here the x axis is chosen as the transport direction, which has an angle α with the armchair direction (the X axis). The electric potential $U(\mathbf{r})$ and vector potential $\mathbf{A}(\mathbf{r})$ induced by the FMG are uniform along the y axis (the normal of the cross

section) but vary along the x direction. The Landau gauge is adopted for the vector potential, $\mathbf{A}(\mathbf{r}) = A_y(x)\mathbf{e}_y$.

The device Hamiltonian is given by $H = H_0[-i\nabla + \mathbf{A}(\mathbf{r})] + U(\mathbf{r})$. The momentum operator $\hat{\mathbf{p}} = -i\nabla$ along the X and Y axis can be written as $\hat{p}_X = \hat{p}_x \cos \alpha - \hat{p}_y \sin \alpha$ and $\hat{p}_Y = \hat{p}_x \sin \alpha + \hat{p}_y \cos \alpha$. Due to the translational invariance of the system along the y direction, we can write the total electronic wave function as $\Psi(\mathbf{r}) = \exp(iqy)\psi_q(x)$, where q is the transverse wave vector, and $\psi_q(x)$ satisfies a one-dimensional Schrödinger equation $H_q^{1D}\psi_q(x) = E\psi_q(x)$. The reduced Hamiltonian H_q^{1D} reads

$$H_q^{1D} = H_0[-i\partial_x \cos \alpha - q_A(x) \sin \alpha, -i\partial_x \sin \alpha + q_A(x) \cos \alpha] + U(x)\sigma_0, \quad (8)$$

where σ_0 is a unit matrix and $q_A(x) = q + A_y(x)$.

To demonstrate the principle of the proposed device, we take a simplified profile for the magnetic-electric barrier: $A_y(x) = A_0[\Theta(x) - \Theta(x - L)]$ and $U(x) = U_0[\Theta(x) - \Theta(x - L)]$, where $\Theta(x)$ is the Heaviside step function, and A_0 and U_0 are the height of the magnetic and electric barrier. Then the device can be divided into three regions: left lead (I), barrier region (II), and right lead (III). In each region $j \in \{I, II, III\}$, $U(x)$ and $q_A(x)$ take constant values $U^{(j)}$ and $q_A^{(j)}$. For a given energy E and wave vector q , the plane-wave solution in region j can be determined from Eqs. (3) and (4) with the replacement

$$\begin{aligned} k_X &\rightarrow k_x^{(j)} \cos \alpha - q_A^{(j)} \sin \alpha, \\ k_Y &\rightarrow k_x^{(j)} \sin \alpha + q_A^{(j)} \cos \alpha, \\ E &\rightarrow E - U^{(j)}. \end{aligned}$$

Here the longitudinal wave vector $k_x^{(j)}$ is unknown, which satisfies

$$a_4(k_x^{(j)})^4 + a_3(k_x^{(j)})^3 + a_2(k_x^{(j)})^2 + a_1 k_x^{(j)} + a_0 = 0, \quad (9)$$

where

$$\begin{aligned} a_4 &= (1 + \gamma - F)^2, \quad F = \cos^2 \alpha + \gamma \sin^2 \alpha, \\ a_3 &= 2(1 - \gamma)(1 + \gamma - F) \sin(2\alpha) q_A^{(j)}, \\ a_2 &= [2\gamma + 1.5(1 - \gamma)^2 \sin^2(2\alpha)] (q_A^{(j)})^2 \\ &\quad + (1 + 2\gamma E_{gh}) \cos^2 \alpha + 2E_{gh} \sin^2 \alpha, \\ a_1 &= 2(1 - \gamma)F \sin(2\alpha) (q_A^{(j)})^3 \\ &\quad - \sin(2\alpha)[1 + 2E_{gh}(\gamma - 1)] q_A^{(j)}, \\ a_0 &= F^2 (q_A^{(j)})^4 + (\sin^2 \alpha + 2E_{gh}F) (q_A^{(j)})^2 \\ &\quad + E_{gh}^2 - (E - U^{(j)})^2. \end{aligned}$$

A solution of Eq. (9) gives a propagating ($\Im k_x^{(j)} = 0$) or decaying ($\Im k_x^{(j)} \neq 0$) mode $u(\mathbf{k}^{(j)}; E - U^j) \exp(ik_x^{(j)}x)$ with $\mathbf{k}^{(j)} = k_x^{(j)}\mathbf{e}_x + q\mathbf{e}_y$. For a propagating mode, the propagating direction is determined by the velocity component $v_x(\mathbf{k}^{(j)}, E) = \mathbf{v}(\mathbf{k}^{(j)}; E) \cdot \mathbf{e}_x$. From Eq. (9) one can obtain four solutions for $k_x^{(j)}$, which are denoted as $k_{x;\beta}^{(j)}$, $\beta \in \{1, 2, 3, 4\}$. The first two solutions bring either right-propagating [$\Im k_x^{(j)} = 0$ and $v_x(\mathbf{k}^{(j)}, E) > 0$] or right-decaying

($\Im k_x^{(j)} > 0$) modes. The last two solutions yield either left-propagating [$\Im k_x^{(j)} = 0$ and $v_x(\mathbf{k}^{(j)}, E) < 0$] or left-decaying ($\Im k_x^{(j)} < 0$) modes.

The wave function in region j can be written as

$$\psi_q^{(j)}(x) = \sum_{\beta=1}^4 c_{\beta}^{(j)} u(\mathbf{k}_{\beta}^{(j)}; E - U^j) \exp(ik_{x,\beta}^{(j)}x). \quad (10)$$

Consider the case that the left region allows N_q right-propagating modes ($1 \leq N_q \leq 2$). For the incidence of an electron from a right-propagating mode with index $b \leq N_q$ in the left lead, one can set the scattering boundary condition as $c_b^{(I)} = 1$, $c_{3-b}^{(I)} = 0$, $c_{3,4}^{(III)} = 0$. The other eight coefficients $c_{\beta}^{(j)}$ can be obtained from the continuity of the wave function and its derivative, $\psi_q^{(I)}|_{x=0} = \psi_q^{(II)}|_{x=0}$, $\partial_x \psi_q^{(I)}|_{x=0} = \partial_x \psi_q^{(II)}|_{x=0}$, $\psi_q^{(II)}|_{x=L} = \psi_q^{(III)}|_{x=L}$, $\partial_x \psi_q^{(II)}|_{x=L} = \partial_x \psi_q^{(III)}|_{x=L}$. We then yield the transmission probability from the right-propagating mode b in the left lead to the right-propagating mode a in the right lead:

$$T_{ab}(E, q) = |c_a^{(III)}|^2 v_x(\mathbf{k}_a^{(III)}, E) / v_x(\mathbf{k}_b^{(I)}, E). \quad (11)$$

For the system with Fermi energy E_F and at zero temperature, the valley-resolved conductance is given by

$$G_{\eta, \eta'}(E_F) = \frac{2e^2}{h} \int \frac{dq}{2\pi/L_y} \sum_{a,b} T_{ab}(E_F, q) \times I_{\eta}(\mathbf{k}_a^{(III)}, E_F) I_{\eta'}(\mathbf{k}_b^{(I)}, E_F), \quad (12)$$

where L_y is the system size along the y direction, and $\eta, \eta' \in \{+1, -1\}$. The valley indicator $I_{\eta}(\mathbf{k}, E) = [\text{sgn}(m_z(\mathbf{k}, E)) + \eta]/2$ takes 1 when the OMM of the propagating state (\mathbf{k}, E) in the lead is along the direction $\eta \mathbf{e}_z$. We define the valley polarization as

$$P_V = \frac{G_{+1} - G_{-1}}{G_{+1} + G_{-1}}, \quad (13)$$

where $G_{\eta} = G_{\eta,+1} + G_{\eta,-1}$. Hereafter, the unit of the conductance is taken as $G_0 = (e^2/h)L_y/(\pi l_0)$. From the view of OMM carried by the output current, the valley polarization can be defined as

$$P_V = - \frac{\int dq \sum_{a,b} T_{ab}(E_F, q) m_z(\mathbf{k}_a^{(III)}, E_F)}{\int dq \sum_{a,b} T_{ab}(E_F, q) |m_z(\mathbf{k}_a^{(III)}, E_F)|}. \quad (14)$$

Here the factor -1 accounts for the fact that $m_z(\mathbf{k}, E)$ is negative for electrons in the conduction band with momentum \mathbf{k} near the valley point \mathbf{D}_+ . We have checked numerically that the two definitions are identical when $\delta \ll |E_F|$.

III. RESULTS AND DISCUSSIONS

A. Transport under a pure electric barrier

For a pure electric barrier ($A_0 = 0$) and the transport along the zigzag direction ($\alpha = 90^\circ$), the valley filtering has been investigated in Ref. [30]. However, the effect of barrier orientation α on the valley polarization P_V has not been explored. In Fig. 2(a) we plot the variation of P_V with the angle α and the barrier height U_0 for a typical Fermi energy $E_F = 0.06$.

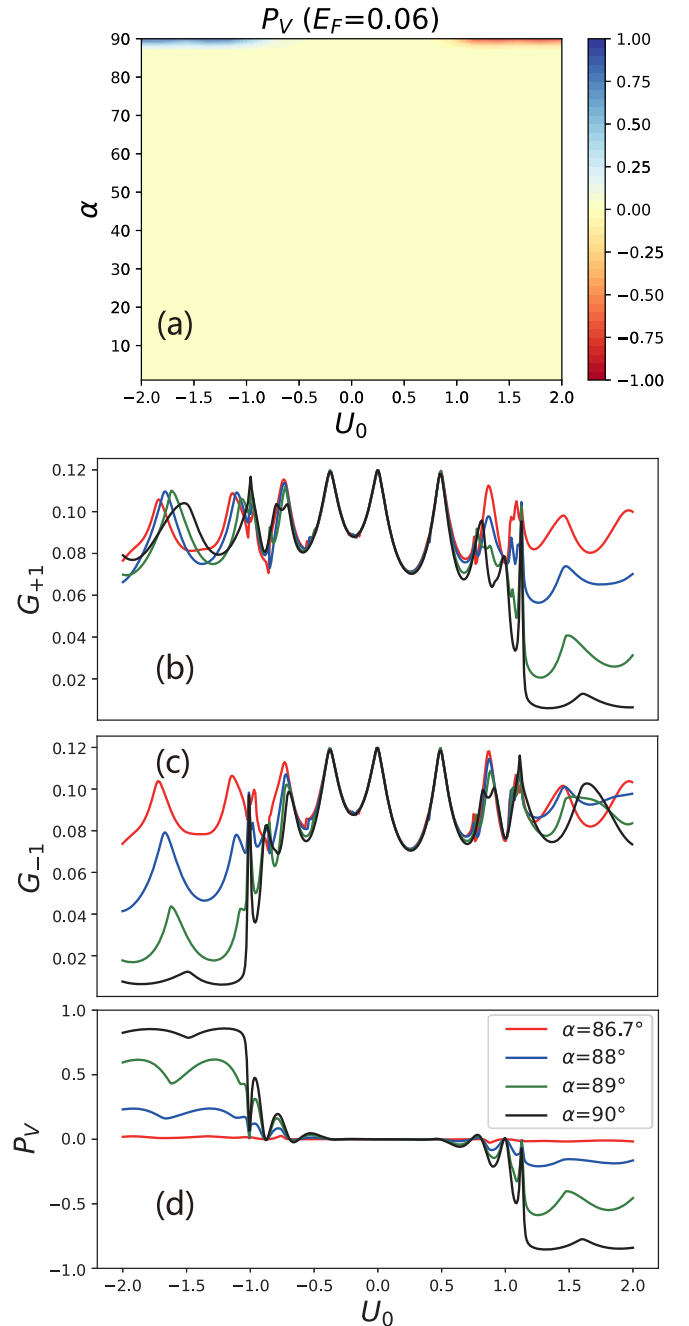


FIG. 2. (a) Valley polarization P_V as a function of the barrier orientation α and the electric barrier height U_0 . [(b)–(d)] Valley-resolved conductance G_{+1} , G_{-1} and valley polarization P_V as a function of U_0 for several barrier orientations, $\alpha = 86.7^\circ$ (red), 88° (blue), 89° (green), and 90° (black). The barrier width and Fermi energy are fixed at $L = 15$ and $E_F = 0.06$. The parameters in Hamiltonian (2) are taken as $\gamma = 5.2$ and $E_{hg} = -1.115$.

The barrier width is set at $L = 15$ (i.e., 12.2 nm). It is seen that for $\alpha \in [89^\circ, 90^\circ]$ a remarkable and positive (negative) P_V happens when $U_0 \in [-2, -1.055]$ ($U_0 \in [1.175, 2]$). In the case that $0 \leq \alpha \leq 86.7^\circ$ or $-0.9 < U_0 < 0.8$, the valley polarization is weak.

To demonstrate more clearly the strong dependence of P_V on the angle α , in Figs. 2(b), 2(c), and 2(d) we plot the

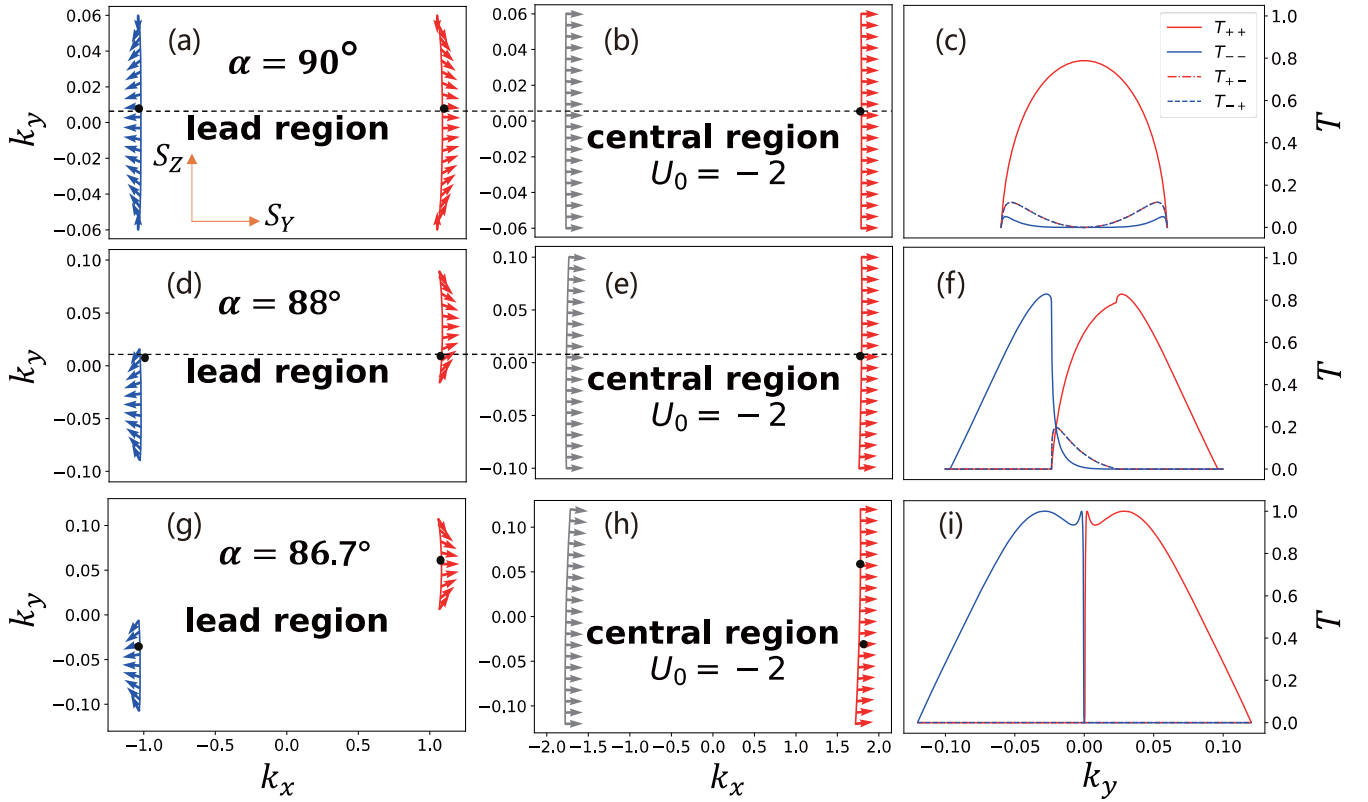


FIG. 3. Left panels: Pseudospin vector of all right-propagating modes in the lead region. Middle panels: Pseudospin vector of left-propagating (in black) and right-propagating (in red) modes in the central region. Right panels: Variation of the transmission probability T_{ab} with the transverse wave vector k_y . We take $U_0 = -2$ and set the angle α as [(a)–(c)] 90° , [(d)–(f)] 88° , and [(g)–(i)] 86.7° .

variation of $G_{\pm 1}$ and P_V with the barrier height U_0 under different values α close to 90° . The curve for $\alpha = 90^\circ$ has the same features as in Ref. [30], although we adopt a different definition of the valley polarization P_V and consider the additional parabolic term $\gamma k_x^2 \sigma_z$. There exist three intervals of U_0 (or gate voltage) where P_V is respectively close to -1 , 0 , and 1 . As suggested in Ref. [30], the three stable valley states can be used to design various Boolean logics. When α changes from 90° to 86.7° , the discrimination among three valley states becomes weaker and weaker. With this decrease of α , the conductance G_{+1} under $U_0 < -0.9$ changes slightly (the minimum changes from 0.066 to 0.079), while G_{-1} increases quickly (the minimum changes from 0.006 to 0.079). As shown in Appendix A, the additional parabolic term has a minor effect on P_V but is not negligible for the two conductances $G_{\pm 1}$. The features in Fig. 2 can be understood from the pseudospin and momentum matching. For an electron traversing the barrier, a remarkable transmission requires the coexistence of right-propagating modes in the lead and in the central region and the matching between their pseudospins. For the incident energy $E = 0.06$, in Fig. 3 we plot the pseudospins of right-propagating modes in the lead and in the central region. The horizontal lines represent the conservation of transverse momentum k_y [k_y is identical to q in Eq. (8)]. Since the conductance is calculated in the zero-bias limit and the two leads have the same dispersion relation, the right-propagating modes in the two leads share the same pseudospin features. It is seen that the sector of allowed transverse momentum in the leads depends on the barrier orientation.

For $\alpha = 90^\circ$ [Fig. 3(a)], k_y varies from -0.06 to 0.06 for both branches. In the central region under $U_0 = -2$ [Fig. 3(b)], there is only one right-propagating mode which we denote as ψ_{rp}^{II} . This state is near the D_+ valley and has a pseudospin aligned mainly to the $+Y$ direction, which coincides with the transport direction for $\alpha = 90^\circ$. In the left lead, the pseudospin of the right-propagating mode near the D_+ (D_-) valley [denoted as $\psi_{rp}^{I,+}$ and $\psi_{rp}^{I,-}$] is nearly parallel (antiparallel) with that of ψ_{rp}^{II} . In this case, electrons incident from the mode $\psi_{rp}^{I,-}$ ($\psi_{rp}^{I,+}$) will be reflected (unhindered) by the barrier, leading to a suppressed G_{-1} (noticeable G_{+1}). In Fig. 3(c) we also plot the variation of the transmission probability T_{ab} with the transverse wave vector k_y . It is seen that the intravalley transmission T_{++} for D_+ valley is much larger than that for D_- valley (i.e., T_{--}). The two intervalley transmissions T_{+-} and T_{-+} are identical, which exceeds T_{--} but is much smaller than T_{++} .

For the barrier orientation $\alpha = 88^\circ$ [Fig. 3(d)], k_y varies from -0.1 to 0.1 . The pseudospin of ψ_{rp}^{II} at $U_0 = -2$ is still close to the $+Y$ axis and has a small but finite angle. In the case $|k_y| < 0.023$, there are two right-propagating modes in the left lead. It can be seen from Fig. 3(f) that in this k_y interval, intervalley transmission can be comparable to intravalley transmission. In the case of $|k_y| > 0.023$, there is only one right-propagating mode in the left lead. Consequently, intervalley transmission is strictly forbidden due to the momentum conservation [31]. For $k_y > 0.023$, intravalley transmission T_{++} is remarkable and meets the rule of pseudospin match.

For $k_y < -0.023$, intravalley transmission T_{--} is also noticeable. The mechanism of pseudospin-selective tunneling found in Ref. [30] is no longer valid when the pseudospin in the scattering region deviates from the transport direction. This feature is more obvious for the barrier orientation $\alpha = 86.7^\circ$ [Figs. 3(g)–3(i)], where only one right-propagating mode exists in the left lead for each allowed k_y . In this case, the intravalley transmission T_{++} and T_{--} are nearly symmetric with respect to the line $k_y = 0$. This fact together with the absence of intervalley transmission results in a tiny P_V .

B. Transport under a magnetic-electric barrier

As mentioned above, a remarkable valley polarization under a pure electric barrier can only be obtained for the transport direction close to the zigzag direction (α near 90°). It is desirable to achieve a gate control of valley polarization for a broad range of transport directions. We note that when the transport is along the armchair direction ($\alpha = 0^\circ$), the valley polarization P_V always vanishes because the system is invariant under the reflection $R_Y : Y \rightarrow -Y$. This symmetry results in the constrain $T_{--}(E, k_y) = T_{++}(E, -k_y)$. To get a finite P_V for $\alpha = 0$, one should break the reflection symmetry R_Y . This can be realized by the application of a magnetic barrier in the scattering region depicted in Fig. 1(c). Hereafter we consider a rectangular magnetic barrier with height $A_0 = 0.054$.

For the considered magnetic-electric barrier, the valley polarization P_V is plotted in Fig. 4(a) as a function of the angle α and the barrier height U_0 . The Fermi energy is also fixed at $E_F = 0.06$. In the case $\alpha \in [89^\circ, 90^\circ]$, the valley polarization generated by the device exceeds 0.8 in amplitude for $U_0 < -1.055$ and $U_0 > 1.175$, which is positive for $U_0 < -1.055$ and negative for $U_0 > 1.175$. In the case $\alpha \in [0^\circ, 35^\circ]$, the valley polarization alternates its polarity with the increasing of U_0 , whose amplitude in both polarities can exceed 0.5. For other transport directions, the valley polarization is finite but not remarkable.

In Figs. 4(b)–4(d) we plot the variation of $G_{\pm 1}$ and P_V with the barrier height U_0 when $\alpha = 90^\circ$ (zigzag) or $\alpha = 70^\circ$ or 0° (armchair). In the case $\alpha = 90^\circ$ and $U_0 < -1.055$, the conductance G_{+1} oscillates above the value 0.077, while G_{-1} is lower than 0.013. Accordingly, the valley polarization P_V is positive and exceeds 0.8. Under $U_0 > 1.175$, the roles of G_{+1} and G_{-1} exchange, leading to a negative P_V with value below -0.8 . Similar to the case of a pure electric barrier ($A_0 = 0$), there still exist three stable valley states where P_V is respectively close to -1 , 0 , and 1 in three intervals of gate voltage. This fact indicates that the required valley states survive under the magnetic barrier. In the case $\alpha = 0^\circ$, the conductance $G_{\pm 1}$ shows a valley-resolved oscillation with U_0 . Near some troughs of G_{+1} , the conductance G_{-1} is close to a peak. Accordingly, a negative valley polarization with amplitude $\approx 50\%$ appears (such as at $U_0 = -2, -0.89$, and 0.99). One can also observe a positive valley polarization with amplitude $\approx 50\%$ near some peaks of G_{-1} (such as at $U_0 = -1.2, -0.08, 0.75$, and 1.51). The valley polarization obtained for $\alpha = 0^\circ$ has a distinct voltage dependence in comparison with that for $\alpha = 90^\circ$. In the case $\alpha = 70^\circ$, the conductance G_{+1} and G_{-1} oscillate near the value 0.09 with

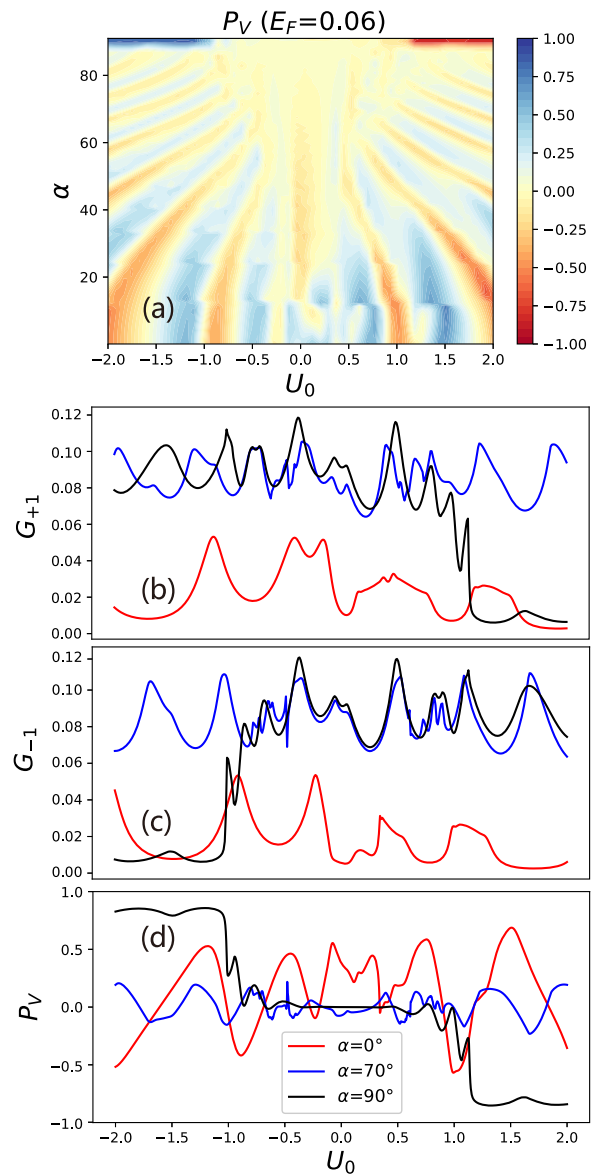


FIG. 4. (a) Valley polarization P_V as a function of the barrier orientation α and the electric barrier height U_0 . (b), (c), (d) Valley-resolved conductance $G_{\pm 1}$ and valley polarization P_V as a function of U_0 for two barrier orientations, $\alpha = 0^\circ$ (red), $\alpha = 70^\circ$ (blue) and 90° (black). We take $A_0 = 0.054$, $E_F = 0.06$, $\gamma = 5.2$, and $E_{hg} = -1.115$.

different patterns, leading to a valley polarization P_V varying between -0.21 and 0.23 .

For the incident energy $E = 0.06$ and magnetic barrier height $A_0 = 0.054$, in Fig. 5 we plot the pseudospins of right-propagating modes in the lead and in the central region ($\psi_{rp}^{I,\pm}$ and ψ_{rp}^{II}) for $\alpha = 90^\circ$ and $\alpha = 0^\circ$. In the case $\alpha = 90^\circ$ [Figs. 5(a)–5(c)], the pseudospin orientation of ψ_{rp}^{II} is almost unaffected by the magnetic barrier. In comparison with Fig. 3(b), the transverse momentum of the propagation mode in Fig. 5(b) is shifted by A_0 along the k_y direction, which leads to a slight change in the transmission. For the barrier orientation $\alpha = 0^\circ$ [Figs. 5(d)–5(f)], the allowed transverse momentum in the left lead is highly concentrated near

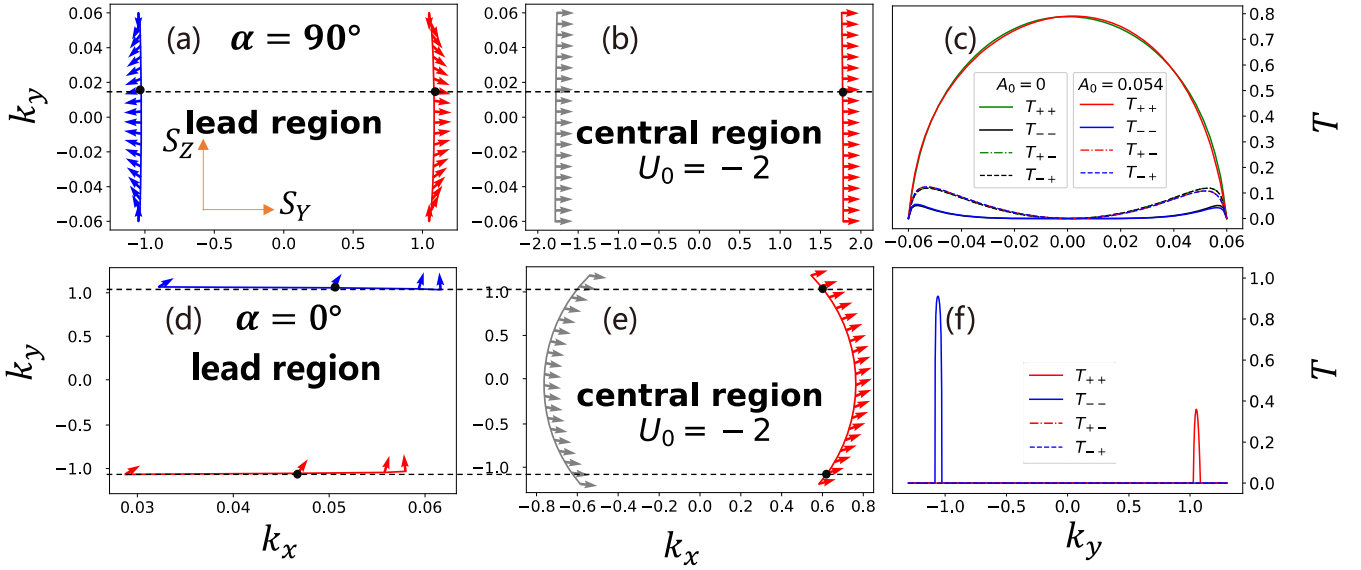


FIG. 5. Left panels: Pseudospin vector of right-propagating modes in the lead region. Middle panels: Pseudospin vector of two propagating modes in the central region. Right panels: Variation of the transmission probability T_{ab} with the transverse wave vector k_y . We take $U_0 = -2$, $A_0 = 0.054$ and set the angle α as [(a)–(c)] 90° and [(d)–(f)] 0° . In (c) the transmission for $A_0 = 0$ is plotted for comparison.

$k_y = \pm k_D$ so that intervalley transmission is forbidden. The pseudospin orientation of $\psi_{rp}^{I,\pm}$ changes from the $+Y$ to the $+Z$ direction as k_x increases. The pseudospin orientations of ψ_{rp}^{II} for all allowed k_y are almost the same but at an angle $\approx 20^\circ$ to the $+Y$ axis. The intravalley transmission T_{--} is finite only for $-1.08 < k_y < -1.03$ and has a maximum of 0.911, while T_{++} has a peak with value 0.36 within $1.03 < k_y < 1.08$. This indicates that the reflection symmetry between the two valleys, i.e., $T_{--}(E, k_y) = T_{++}(E, -k_y)$, is broken effectively by the magnetic barrier with height $A_0 = 0.054$. Such a valley-dependent resonant tunneling can result in a remarkable valley polarization. As shown in Appendixes B and C, the valley polarization at $\alpha = 0^\circ$ depends on the thickness-dependent material parameters and can be enhanced by increasing the height A_0 and width L of the magnetic barrier.

IV. CONCLUSIONS

In summary, we have studied the effect of transport direction on the valley filtering in a band-inverted phosphorene multilayer modulated by either a pure electric barrier or a magnetic-electric barrier. When the pure electric barrier is along the zigzag direction, we have confirmed that the device can undergo three distinct valley states as the barrier height varies. The discrimination among the three valley states diminishes quickly as the transport direction deviates from the zigzag direction. The valley polarization tends to be zero when intervalley transmission is absent, which vanishes strictly for the transport along the armchair direction. When a magnetic barrier is included, the three valley states survive for the transport along the zigzag direction. When the transport direction is near the armchair direction, the valley polarization alternates its sign with the gate voltage and can exceed 50% in amplitude for both polarities. In this case the magnetic barrier effectively breaks the reflection symmetry between the two valleys. Our

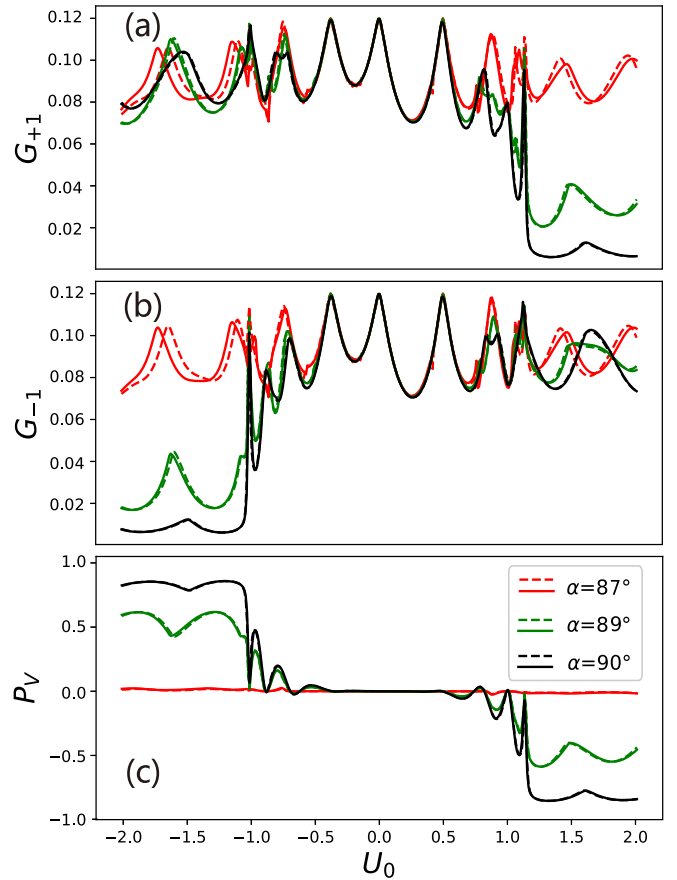


FIG. 6. Valley-resolved conductance $G_{\pm 1}$ [(a) and (b)] and valley polarization P_V [(c)] plotted as functions of the height U_0 of the pure electric barrier with orientation angle $\alpha = 86.7^\circ, 89^\circ, 90^\circ$. The solid lines are for $\gamma = 5.2$, while the dashed lines are for $\gamma = 0$. Other parameters are the same as in Fig. 2.

TABLE I. Inverted gap ε_g , effective velocity v_X , and effective mass m_Y and m_X for three-layered ($N = 3$) and five-layered ($N = 5$) BP nanofilm.

N	v_X (m/s)	ε_g (eV)	m_Y/m_e	m_X/m_e
3, Refs. [44,53]	5.1×10^5	-0.912	1.493	0.169
5, Refs. [56,57]	2.02×10^5	-0.560	1.2	0.17

findings could be helpful for valleytronic applications based on anisotropic 2D systems with band inversion.

ACKNOWLEDGMENT

This work was supported by the National Natural Science Foundation of China (Grant No. 12274370).

APPENDIX A: EFFECT OF ADDITIONAL PARABOLIC TERM

To examine the influence of an additional parabolic term $H_{XX} = \gamma k_X^2 \sigma_Z$ in the Hamiltonian (2), we calculate the conductance G_+ and G_- and valley polarization P_V for the case $\gamma = 5.2$ and $\gamma = 0$. The results for the pure electric barrier are shown in Fig. 6. It can be seen that for the situation $-0.9 < U_0 < 0.8$, the conductance G_{+1} and G_{-1} and thus P_V are almost unchanged by the term H_{XX} . When α decreases from 90° to 86.7° , the inclusion of the term H_{XX} leads to the shift of conductance peaks within $U_0 < -1.055$ or $U_0 > 1.175$ but has a minor effect on the valley polarization P_V .

At a large Fermi energy such as $E_F = 0.2$, our numerical results (not shown here) indicate that the additional parabolic term greatly affects the conductance when the polarization is large in amplitude—it can move a peak of $G_{\pm 1}$ to a trough, and it can also lower the peaks of “minority” conductance by $\approx 20\%$.

APPENDIX B: THREE-LAYERED AND FIVE-LAYERED BP UNDER A MAGNETIC-ELECTRIC BARRIER

It is necessary to explore the effect of the thickness (or the number of layers, N) of multilayer BP on the amplitude of valley polarization. For BP nanofilm, the gap, effective mass, and critical field for band inversion change with the thickness [53,54]. In the case of $N = 3$ and $N = 5$, the relevant material parameters are listed in Table I. Note that the effective velocity v_X for $N = 3$ was not given directly in Ref. [44]. As shown in Ref. [27] [see Fig. 3(d) therein], v_X changes only slightly after the band closure. We thus take $v_X = 5.1 \times 10^5$ m/s for $N = 3$ based on Ref. [44]. In order to generate an inverted band gap, we take the critical gate density $n_c = 18 \times 10^{13}$ cm $^{-2}$ for the case $N = 3$, which gives $\varepsilon_g = -0.912$ eV [54,55]. For the chosen material parameters, the highest energy of the inverted band (in units of $\varepsilon_0 = 2m_Y v_X^2$) is $|E_{hg}| = |\varepsilon_g|/(2\varepsilon_0) = 0.155$ (0.503) for $N = 3$ ($N = 5$) where $\varepsilon_0 = 2.928$ eV (0.5568 eV).

In Fig. 7 the valley polarization P_V is plotted for the trilayer and five-layered BP under the magnetic-electric barrier with width $L = 15$ and height $A_0 = 0.054$. The Fermi energy is taken as $E_F = 0.06$, which is lower than $|E_{hg}|$ in both cases.

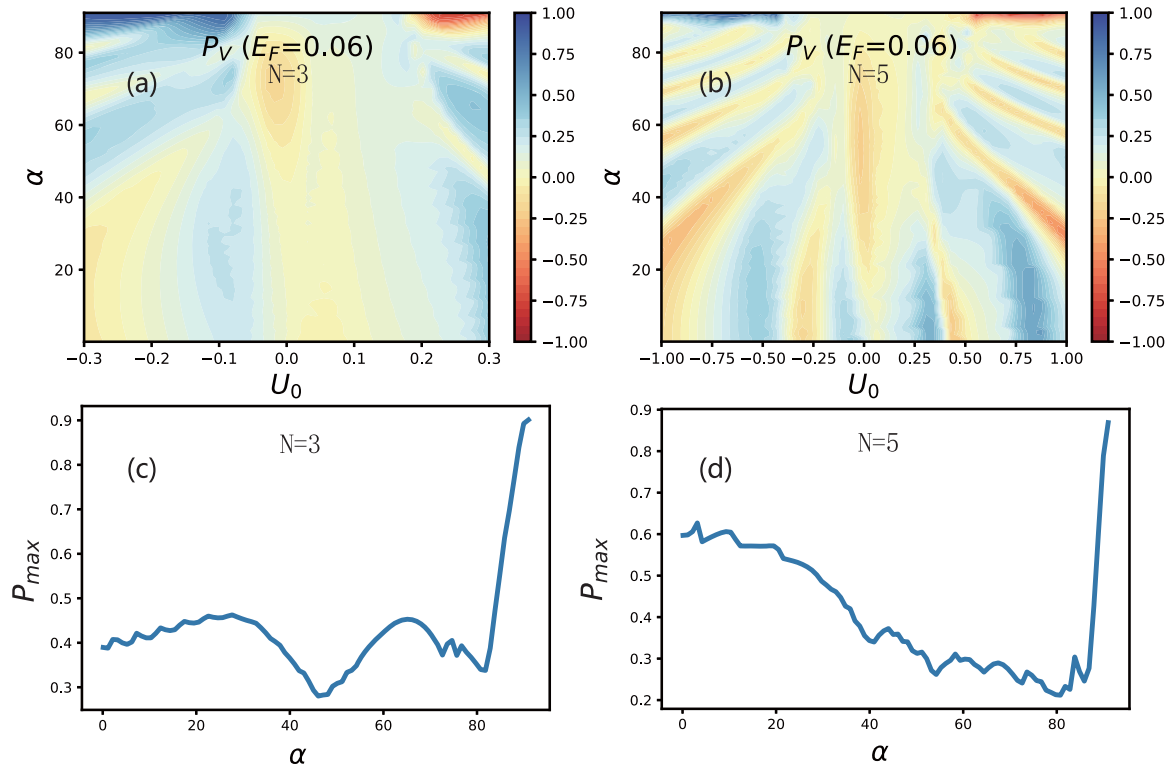


FIG. 7. Valley polarization P_V for a three-layered ($N = 3$) and five-layered ($N = 5$) BP nanofilm under $A_0 = 0.054$, $L = 15$, and $E_F = 0.06$. (a), (b) Valley polarization P_V as a function of barrier height U_0 and orientation α . (c), (d) Maximum P_{\max} of valley polarization attainable by tuning the electric barrier, plotted as a function of barrier orientation α . The relevant material parameters are given in Table I.

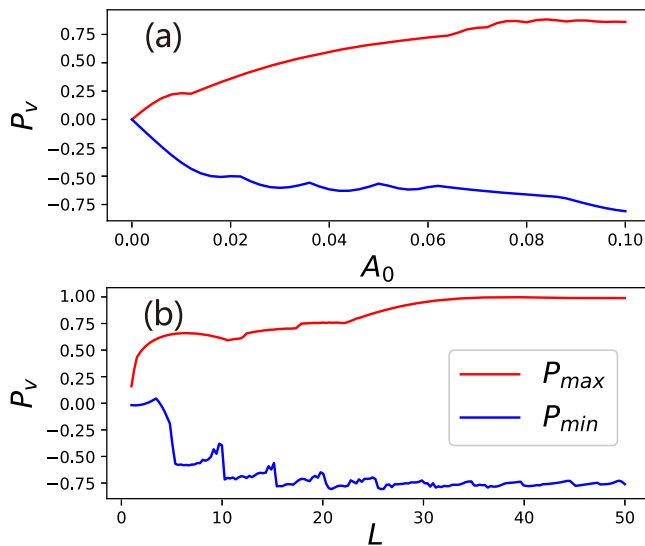


FIG. 8. Maximum and minimum of valley polarization attainable by tuning the electric barrier are plotted as a function of the (a) height A_0 and (b) width L of the magnetic barrier. In (a) we take $L = 15$. In (b) we set $A_0 = 0.054$. Other parameters are the same as in Fig. 2.

In comparison with the case $N = 4$ [see Figs. 4(a), 7(a), and 7(b)], one can see that the three stable valley states survive in a broader interval of orientation (near $\alpha = 90^\circ$) for the case $N = 3$. In addition, near $\alpha = 0$ the valley polarization for trilayer BP is weaker than that for the case of $N = 4, 5$. The possible reason is that $E_F/|E_{hg}|$ for $N = 3$ is the largest. The variation of P_V with α and U_0 for five-layered BP is similar to the case of $N = 4$ in the text, where many traces of zero polarization can be observed.

In Figs. 7(c) and 7(d) we plot the maximum P_{max} of valley polarization attainable by tuning the electric barrier as a

function of the orientation α . In the case $N = 3$, P_{max} is close to 0.4 under $\alpha = 0$ and reaches a global minimum of 0.28 near $\alpha = 45^\circ$. In this case, P_{max} approaches 0.9 at $\alpha = 90^\circ$. In the case $N = 5$, P_{max} is close to 0.6 under $\alpha = 0$ and reaches 0.87 at $\alpha = 90^\circ$. The global minimum of P_{max} , however, locates at $\alpha = 80^\circ$ (close to the zigzag direction) and is lower than that for $N = 3$. The maximum of P_{max} is 0.9 (0.87) under $N = 3$ ($N = 5$), which is larger than the counterpart (0.8) under $N = 4$. This comparison indicates that the magnitude of valley polarization can be further improved by changing the thickness-dependent material parameters such as the inverted gap, effective mass, and effective velocity.

APPENDIX C: EFFECT OF THE HEIGHT AND WIDTH OF THE MAGNETIC BARRIER

To investigate the effect of barrier parameters on the valley polarization, in Fig. 8 we plot the maximum and minimum of valley polarization (P_{max} and P_{min}) attainable by tuning the electric barrier, which depends on the height A_0 and width L of the magnetic barrier. Here the TBP is considered and the barrier orientation is fixed at $\alpha = 0^\circ$. Other parameters are the same as Fig. 2. In Fig. 8(a) where L is fixed at 15, one can see that the maximum P_{max} (minimum P_{min}) of valley polarization has value 0 at $A_0 = 0$ and gradually reaches 0.88 (-0.8) as A_0 increases. In Fig. 8(b) where A_0 is set at 0.054, it can be seen that the maximum P_{max} (minimum P_{min}) increases initially with the width L and then approaches 1 (-0.8) with a small fluctuation (several drops). Therefore the maximum amplitude of attainable valley polarization can be enhanced by tuning either the height A_0 or width L of the magnetic barrier. The reason is that the valley-related momentum filtering for $\alpha = 0^\circ$ due to the magnetic barrier is more remarkable under larger A_0 and L .

- [1] S. A. Vitale, D. Nezich, J. O. Varghese, P. Kim, N. Gedik, P. Jarillo-Herrero, D. Xiao, and M. Rothschild, *Small* **14**, 1801483 (2018).
- [2] J. R. Schaibley, H. Yu, G. Clark, P. Rivera, J. S. Ross, K. L. Seyler, W. Yao, and X. Xu, *Nat. Rev. Mater.* **1**, 16055 (2016).
- [3] T. Cao, G. Wang, W. Han, H. Ye, C. Zhu, J. Shi, Q. Niu, P. Tan, E. Wang, B. Liu, and J. Feng, *Nat. Commun.* **3**, 887 (2012).
- [4] K. F. Mak, K. He, J. Shan, and T. F. Heinz, *Nat. Nanotechnol.* **7**, 494 (2012).
- [5] H. Zeng, J. Dai, W. Yao, D. Xiao, and X. Cui, *Nat. Nanotechnol.* **7**, 490 (2012).
- [6] L. Li, L. Shao, X. Liu, A. Gao, H. Wang, B. Zheng, G. Hou, K. Shehzad, L. Yu, F. Miao, Y. Shi, Y. Xu, and X. Wang, *Nat. Nanotechnol.* **15**, 743 (2020).
- [7] R. V. Gorbachev, J. C. W. Song, G. L. Yu, A. V. Kretinin, F. Withers, Y. Cao, A. Mishchenko, I. V. Grigorieva, K. S. Novoselov, L. S. Levitov, and A. K. Geim, *Science* **346**, 448 (2014).
- [8] Y. Shimazaki, M. Yamamoto, I. V. Borzenets, K. Watanabe, T. Taniguchi, and S. Tarucha, *Nat. Phys.* **11**, 1032 (2015).
- [9] F. Zhai, X. Zhao, K. Chang, and H. Q. Xu, *Phys. Rev. B* **82**, 115442 (2010).
- [10] F. Zhai, Y. Ma, and Y.-T. Zhang, *J. Phys.: Condens. Matter* **23**, 385302 (2011).
- [11] C.-C. Hsu, M. L. Teague, J.-Q. Wang, and N.-C. Yeh, *Sci. Adv.* **6**, eaat9488 (2020).
- [12] T. Fujita, M. B. A. Jalil, and S. G. Tan, *Appl. Phys. Lett.* **97**, 043508 (2010).
- [13] F. Zhai and K. Chang, *Phys. Rev. B* **85**, 155415 (2012).
- [14] G. Giovannetti, P. A. Khomyakov, G. Brocks, P. J. Kelly, and J. van den Brink, *Phys. Rev. B* **76**, 073103 (2007).
- [15] D. Gunlycke and C. T. White, *Phys. Rev. Lett.* **106**, 136806 (2011).
- [16] J.-H. Chen, G. Autès, N. Alem, F. Gargiulo, A. Gautam, M. Linck, C. Kisielowski, O. V. Yazyev, S. G. Louie, and A. Zettl, *Phys. Rev. B* **89**, 121407(R) (2014).
- [17] C. Park, *Phys. Rev. Appl.* **11**, 044033 (2019).
- [18] J. Zheng, J. Lu, and F. Zhai, *Phys. Rev. B* **105**, 165410 (2022).
- [19] M. S. Mrudul, Á. Jiménez-Galán, M. Ivanov, and G. Dixit, *Optica* **8**, 422 (2021).

- [20] F. Caruso, M. Schebek, Y. Pan, C. Vona, and C. Draxl, *J. Phys. Chem. Lett.* **13**, 5894 (2022).
- [21] X. Wang, Y. Sun, and K. Liu, *2D Mater.* **6**, 042001 (2019).
- [22] K. Dolui and S. Y. Quek, *Sci. Rep.* **5**, 11699 (2015).
- [23] S. Kuriakose, T. Ahmed, S. Balendhran, G. E. Collis, V. Bansal, I. Aharonovich, S. Sriram, M. Bhaskaran, and S. Walia, *Appl. Mater. Today* **12**, 244 (2018).
- [24] J. Qiao, X. Kong, Z. X. Hu, F. Yang, and W. Ji, *Nat. Commun.* **5**, 4475 (2014).
- [25] V. Tran, R. Soklaski, Y. Liang, and L. Yang, *Phys. Rev. B* **89**, 235319 (2014).
- [26] C. Wang, G. Zhang, S. Huang, Y. Xie, and H. Yan, *Adv. Opt. Mater.* **8**, 1900996 (2020).
- [27] J. Jang, S. Ahn, and H. Min, *2D Mater.* **6**, 025029 (2019).
- [28] J. Kim, S. S. Baik, S. W. Jung, Y. Sohn, S. H. Ryu, H. J. Choi, B.-J. Yang, and K. S. Kim, *Phys. Rev. Lett.* **119**, 226801 (2017).
- [29] S. S. Baik, K. S. Kim, Y. Yi, and H. J. Choi, *Nano Lett.* **15**, 7788 (2015).
- [30] Y. S. Ang, S. A. Yang, C. Zhang, Z. Ma, and L. K. Ang, *Phys. Rev. B* **96**, 245410 (2017).
- [31] Y. W. Choi, *2D Mater.* **8**, 035024 (2021).
- [32] H.-Y. Mu, N.-W. Wang, Y.-N. Du, X.-T. An, and J.-J. Liu, *Phys. Rev. B* **105**, 115305 (2022).
- [33] S. Bhowal and G. Vignale, *Phys. Rev. B* **103**, 195309 (2021).
- [34] G. Montambaux, F. Piéchon, J. N. Fuchs, and M. O. Goerbig, *Eur. Phys. J. B* **72**, 509 (2009).
- [35] L.-K. Lim, J.-N. Fuchs, and G. Montambaux, *Phys. Rev. Lett.* **108**, 175303 (2012).
- [36] L. Li, J. Kim, C. Jin, G. J. Ye, D. Y. Qiu, F. H. Da Jornada, Z. Shi, L. Chen, Z. Zhang, F. Yang *et al.*, *Nat. Nanotechnol.* **12**, 21 (2017).
- [37] G. Zhang, S. Huang, A. Chaves, C. Song, V. O. Özçelik, T. Low, and H. Yan, *Nat. Commun.* **8**, 14071 (2017).
- [38] R. Fei, V. Tran, and L. Yang, *Phys. Rev. B* **91**, 195319 (2015).
- [39] Z. J. Xiang, G. J. Ye, C. Shang, B. Lei, N. Z. Wang, K. S. Yang, D. Y. Liu, F. B. Meng, X. G. Luo, L. J. Zou, Z. Sun, Y. Zhang, and X. H. Chen, *Phys. Rev. Lett.* **115**, 186403 (2015).
- [40] A. S. Rodin, A. Carvalho, and A. H. Castro Neto, *Phys. Rev. Lett.* **112**, 176801 (2014).
- [41] Q. Liu, X. Zhang, L. Abdalla, A. Fazzio, and A. Zunger, *Nano Lett.* **15**, 1222 (2015).
- [42] S. Yuan, E. van Veen, M. I. Katsnelson, and R. Roldán, *Phys. Rev. B* **93**, 245433 (2016).
- [43] H. Doh and H. J. Choi, *2D Mater.* **4**, 025071 (2017).
- [44] J. Kim, S. S. Baik, S. H. Ryu, Y. Sohn, S. Park, B.-G. Park, J. Denlinger, Y. Yi, H. J. Choi, and K. S. Kim, *Science* **349**, 723 (2015).
- [45] N. Ehlen, A. Sanna, B. V. Senkovskiy, L. Petaccia, A. V. Fedorov, G. Profeta, and A. Grüneis, *Phys. Rev. B* **97**, 045143 (2018).
- [46] D. Xiao, J. Shi, and Q. Niu, *Phys. Rev. Lett.* **95**, 137204 (2005).
- [47] D. Xiao, M.-C. Chang, and Q. Niu, *Rev. Mod. Phys.* **82**, 1959 (2010).
- [48] T. Thonhauser, D. Ceresoli, D. Vanderbilt, and R. Resta, *Phys. Rev. Lett.* **95**, 137205 (2005).
- [49] A. Nogaret, *J. Phys.: Condens. Matter* **22**, 253201 (2010).
- [50] A. Tarasov, S. Hugger, H. Xu, M. Cerchez, T. Heinzl, I. V. Zozoulenko, U. Gasser-Szerer, D. Reuter, and A. D. Wieck, *Phys. Rev. Lett.* **104**, 186801 (2010).
- [51] A. Leuschner, J. Schluck, M. Cerchez, T. Heinzl, K. Pierz, and H. W. Schumacher, *Phys. Rev. B* **95**, 155440 (2017).
- [52] M. Cerchez, T. Chirila, H. Bettermann, B. Schüler, and T. Heinzl, *Phys. Rev. B* **99**, 085303 (2019).
- [53] D. J. P. de Sousa, L. V. de Castro, D. R. da Costa, J. M. Pereira, and T. Low, *Phys. Rev. B* **96**, 155427 (2017).
- [54] J. D. Forte, D. J. de Sousa, and J. M. Pereira, *Physica E* **114**, 113578 (2019).
- [55] K. Dolui and S. Y. Quek, *Sci. Rep.* **6**, 25429 (2016).
- [56] W. J. Chan, L. K. Ang, and Y. S. Ang, *Appl. Phys. Lett.* **122**, 163102 (2023).
- [57] B. Ghosh, B. Singh, R. Prasad, and A. Agarwal, *Phys. Rev. B* **94**, 205426 (2016).